Dimensional Effects of Polymer Piezoelectric Films for Wind Energy Harvesting

Phillip C. Scott
Mechanical Engineering Department,
University of New Mexico,
Albuquerque, NM 87131

Nathan Jackson
Mechanical Engineering Department,
University of New Mexico,
Albuquerque, NM 87131

Svetlana V. Poroseva
Mechanical Engineering Department,
University of New Mexico,
200 University Blvd., MSC01 1150,
Albuquerque, NM 87131
e-mail: poroseva@unm.edu

Arrays of flexible polymer piezoelectric film cantilevers that mimic grass or leaves is a prospective idea for harvesting wind energy in urban areas, where the use of traditional technologies is problematic due to low wind velocities. Conversion of this idea into an economically attractive technology depends on various factors including the shape and dimensions of individual films to maximize generated power and to minimize associated costs of production, operation, and maintenance. The latter requirement can be satisfied with rectangular films undergoing flutter in ambient air. Flexible piezoelectric films that displace due to low forces and can convert mechanical energy into electrical energy are ideal for this application. The goal of the presented study is to determine the key dimensions of the piezoelectric film to enhance generated power within the wind range characteristic for urban areas from 1.3 to 7.6 m/s. For this purpose, experiments were conducted in a wind tunnel using piezoelectric polymer films of polyvinylidine fluoride with the length, width, and thickness varying in the ranges of 32–150, 16–22, and 40–64 μm, respectively. Voltage and power outputs for individual samples were measured at wind speeds ranging from 0.5 to 16.5 m/s. Results demonstrated that a single film could produce up to 0.74 nW and that the optimal film dimensions are 63 mm × 22 mm × 40 μm (from considered samples) for the wind energy harvesting in urban areas. Further improvement in power production can be expected when using films with reduced thickness, low elastic modulus, and increased length, and by assembling films in arrays.
[DOI: 10.1115/1.4053313]

1 Introduction

In recent decades, there has been an increase in the development of renewable energy harvesters, on the scales of both a public utility and a single dwelling. While on the single-dwelling scale, photovoltaic cells constitute the standard for collecting solar energy, no such standard yet exists for wind energy. On the utility scale, large wind turbines are utilized. Their operation requires high consistent wind speed (annual averages of greater than 7.5 m/s) [1]. For this reason, wind turbines are typically placed 80–100 m above ground and are located away from built-up areas [2]. Urban cities have much lower wind speeds of the order of 2–5 m/s range and up to 7.6 m/s in extreme conditions [3], which makes the use of wind turbines in an urban or suburban area impractical. Therefore, new energy harvesting technologies are required to harvest urban wind. One possible means is using piezoelectric materials that rely on flutter to extract the wind energy by converting mechanical displacement caused from the wind into usable electrical energy. This is the area of interest for the current study.

Aeroelastic flutter is an instability in a flexible material excited by the flow of a fluid in which the material is immersed. It was first investigated with the aim of preventing violent oscillations leading to catastrophic structural failures [4,5]. Recently, research has been conducted with the purpose of intentionally initiating flutter to harvest kinetic energy from a fluid flow using custom-designed structures [6–23].

The two means of initiating flutter are extraneously induced excitation (EIE) and movement-induced excitation (MIE). In EIE, flutter is induced and sustained in the immersed structure by externally introduced irregularities in the flow, such as the shedding of a von Kármán vortex using a bluff body [24]. One of the earliest flutter-based energy harvesters consisted of a long strip of a flexible piezoelectric polymer made to resemble an eel with a downstream rectangular bluff body [25]. The EIE-based wind harvesting devices using flexible piezoelectrics have also been extensively researched by altering the oscillation direction, tip shapes, and methods of integrating the bluff body [7,11–13,22]. However, the requirement of a bluff body limits the use of the EIE-based devices for wind harvesting in urban areas as it requires a larger footprint area, more complex setup for high density arrays, and only functions with wind blowing in a single direction.

On the other hand, devices designed to undergo MIE are less sensitive to wind direction and no bluff body is required. The piezoelectric films can be manufactured with varying dimensions and shapes and arranged in arrays to increase power generation.

When MIE occurs because of its interaction with an outside body [24], for example, impact with a physically present stopper, such a phenomenon is called coupled MIE [26,27]. A coupled MIE-based device can harvest energy using piezoelectrics or triboelectric effect [8]. No outside body is involved in uncoupled MIE. An example of an uncoupled MIE-based device is a wind energy harvester using a flutter induced flexible belt to excite a magnetic resonator inside an air duct [28].

Most wind harvesting MIE-based devices have directly utilized the electroactive properties of materials, such as piezoelectrics. Piezoelectric energy harvesters operate by converting mechanical strain caused from deformation of the film into usable electrical energy. Apart from piezoelectrics, other electroactive materials have been developed such as flexible ionic polymer metal composite (IPMC) [19]. While the maximum power harvested from the IPMC was 143 nW/mm^3 for a single rectangular strip, these materials operate best in liquid which is not suitable for wind harvesting. Flexible piezoelectric materials have been extensively investigated as low frequency vibration energy harvesting devices for numerous applications [29–31].

There are numerous piezoelectric materials that have been investigated for energy harvesting devices from stiff ceramics like AlN, ZnO, and PZT [30,32]. However, polyvinylidene fluoride (PVDF) is a flexible polymer-based piezoelectric (elastic modulus of 2–4 GPa) that has been used in low frequency applications due

[1]Corresponding author.

Contributed by the Fluids Engineering Division of ASME for publication in the Journal of Fluids Engineering. Manuscript received June 7, 2021; final manuscript received December 10, 2021; published online February 17, 2022. Assoc. Editor: Jun Chen.

to its decreased stiffness. The stiffer ceramic piezoelectric materials typically have higher power densities, but they operate at higher resonant frequency, which makes it difficult to implement in low frequency wind applications without the use of large proof-masses. On the other hand, PVDF has a lower elastic modulus thus allowing it to be used in low frequency applications such as MIE energy harvesters. New flexible polymer-based piezoelectric materials with potentially higher power density than existing PVDF are also under development and could be promising wind harvesting materials in the future [33–35].

Previous attempts to increase power from PVDF-based wind energy harvesting devices have focused on varying the material properties and the shape of the cantilevers including the development of a triangular "leaf" tip [15–17]. The cost, design, and efficiency of such arrays is determined by the shape and dimensions of individual harvesters within an array. Rectangular strips from PVDF (and PZT) were studied in [20]. Other attempts have involved creating curved or buckled beams, but this increases the complexity of the manufacturing process [36,37].

This paper investigates the wind energy harvesting potential of rectangular PVDF cantilevers undergoing the MIE flutter and the effects of varying dimensions of the PVDF films. Simplicity of this shape is attractive for manufacturing and maintenance, and thus, will reduce the device cost and increase its reliability. The considered cantilever dimensions and mechanical properties are comparable to those of grass, as the energy harvester array could mimic artificial grass which is capable of converting wind into usable electrical energy. In the study, the length, width, and thickness of the PVDF film varied with the purpose of selecting a sample capable of producing the highest power output within the broadest range of wind speeds characteristic for urban environments. The paper also investigates the use of both uncoupled and coupled MIE at various wind speeds. The information determined from this study can be used to develop new flexible piezoelectric materials with enhanced properties and integration of high-density piezoelectric arrays.

2 Materials and Methods

2.1 Experimental Setup. For the experiments, the piezoelectric samples were tested in an open-circuit 0.35 HP subsonic wind tunnel (ELD Inc., model 401) (Fig. 1(*a*)). The samples were suspended from the top of the 6-inch square test section of the wind tunnel (Fig. 1(*b*)). The sample wire leads were attached to a Hantek DSO5000P digital storage oscilloscope set to measure voltage at 200 samples per second. A custom-made 3D printed holder was developed to securely fasten the samples to the top of the wind tunnel to minimize wake, vortex, and roughness effects, as shown in Fig. 1(*c*). An air-tight gasket between the clip and the top of the chamber was achieved using an O-ring and rubber cement. The holder and sample were then inserted into the chamber with the aid of a thin layer of petroleum jelly. Each sample was tested at air speeds ranging from 0.51 to 16.47 m/s at intervals of 0.05 m/s. The air speed in the wind tunnel was controlled by a digital panel that varied the fan frequency. In the experiments, the wind tunnel was operated with a fan revolution frequency ranging from 3.0 to 60.0 Hz at intervals of 0.5 Hz.

For each wind speed setting, the oscilloscope display was observed until a steady pattern emerged (approximately 1 min). Then, a 40 s sampling of voltage versus time was recorded. Tests were conducted with five cohorts of rectangular PVDF samples, purchased from TE connectivity. Each sample consisted of a PVDF film with silver ink electrodes printed on each side, and a thin outer protective urethane coating to protect the conducting electrodes. The elastic modulus of the PVDF films was between 2 and 4 GPa, generating a low stiffness to allow the device to operate at low frequencies which is desired for low wind speeds. Wires were attached to each electrode using a rivet bonding method to ensure excessive heating was not applied to the PVDF. The dimensions of each cohort are given in Table 1. In the table, dimensional identifiers take the form of L*xx*-W*xx*-t*xx*, where the digits following the letters *L*, *W*, *t* for the lengths, width, and thickness of the samples, respectively, in mm (length and width) and μm (thickness). All samples of the first four cohorts in the table have the same width. These samples were used to study effects of the length and the thickness on the power outputs. Samples from the cohort identified as L*xx*-W22-t40 were also used to study the sample length effects with varying widths. The samples were cut from a sheet of PVDF using a razor blade to ensure that the top and bottom electrode did not short. The lengths of the films were 150, 130, 120, 110, 95, 90, 80, 70, and 63 mm. When samples from this group are mentioned as having been cut to a specific length, the xx in its dimensional identifier will be replaced with its effective length in mm.

Two sets of tests were conducted for the varying samples. The first set of tests measured the open-circuit voltages produced by samples from all cohorts. These tests had two purposes. One was to gauge the behavior of all samples under consideration in order to determine which would be the most likely candidates for optimal power production experimentation. The second purpose was to determine at which frequencies the peak voltages at each wind speed occurred so that ideal capacitive impedances could be determined for the power measurement test as the load impedance needs to match the device impedance for maximum power efficiency.

The second set of experiments were used to determine power conversion, which consisted of connecting a variable load resistor in series with the PVDF energy harvester. The input impedance was matched to the impedance of the film in order to maximize power. Since peak voltage frequencies (and therefore sample impedance) varied with wind speed, resistances were varied accordingly over the course of each test. The variable parameters of the experiment are summarized in Table 2.

2.2 Data Analysis. In order to identify the flutter type and voltage magnitude from a given sample at a specified wind speed, the data for each test were converted to the frequency domain using a fast Fourier transform. The flutter type was also validated by visual observation of the samples being tested. Specifically, fixed-point stability was determined to have occurred when the sample was observed to be static, swaying gently in the air flow, or undergoing brief, unsustained periods of vibration. It was concluded that limit-cycle oscillations (LCOs) occurred when most of the data collected from a test were confined to a narrow range of frequencies and the sample was observed to be vibrating in a steady, orderly fashion. The presence of chaotic flapping was deduced when the data were scattered across a broad range of frequencies and the sample tip was observed to be moving in a seemingly random, disorderly fashion. In cases where coupled MIE took place, samples were observed to experience repeated impact against the test chamber ceiling under extreme deformation of the cantilever. Previous work has demonstrated that uncoupled MIE occurring in LCO provides the maximum energy transfer from fluid flow to a flexible object [38].

The cohorts and/or cohort variations that produced the most voltage in each category (thickness, width, and length), particularly at wind speeds under 8 m/s, were selected for the second set of tests. The magnitude of the impedance of the films at various wind speed were calculated from the capacitance of the film and the frequency of the peak voltage. In cases, where multiple samples had been tested, f is the mean peak voltage frequency. For samples that had not been cut prior to testing, the manufacturer rated capacitance was used. For samples that had been cut, capacitance was determined according to the following expression:

$$C = C_r \frac{A}{A_0} \tag{1}$$

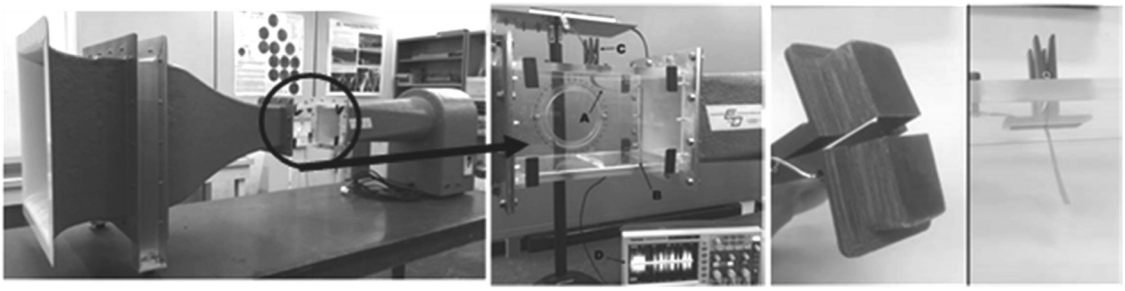

(a) (b) (c)

Fig. 1 Experimental setup. Images: (*a*) wind tunnel, (*b*) test chamber, and (*c*) clip used to fasten a sample to the test chamber and image of the device suspended from top of the wind tunnel.

where C_r is the manufacturer-rated capacitance, A_0 is the area of the uncut sample electrode, and A is the area of a cut sample electrode.

Power, P, generated during the second set of tests was determined as

$$P = \frac{V_{\text{rms}}^2}{R} \tag{2}$$

where V_{rms} is the root-mean-square of the peak voltage generated and R is the resistance added to the circuit to match the impedance. A variable resistor was used to adjust the resistance to within an error of $\pm 0.001\ \text{M}\Omega$. A 60 Hz noise signal caused by the mains electricity used to power the oscilloscope, was present in the testing but had values of < 2 mV and thus became negligible in tests where higher voltages were produced. This phenomenon was mitigated in postprocessing by filtering the frequency range of 59.9–60.1 Hz from all calculations.

3 Results and Discussion

3.1 Characterization of Flutter Stages. In the experiments conducted, the samples underwent three distinct stages of excitation as wind speed increased: fixed-point stability, uncoupled MIE flutter, and coupled MIE flutter driven by percussive impact with the test chamber ceiling surface.

Figure 2 provides an example of voltage variations with time for a sample undergoing different flutter stages. The raw oscilloscope data shown in the figure were collected from Sample 1 of Cohort L63-W16-t40, at wind speed intervals of approximately 1 m/s. The figure does not represent a single experimental run, but rather 500 ms samplings from the experimental runs corresponding to the wind speeds shown in the x-axis. Across the top of the plot are labels indicating the type of flutter (or, in the case of the Fixed-Point Stability here, lack thereof) associated with each wind speed. The data were recorded at a resolution of 1 point every 5 ms. Video is also provided in Supplemental Material to help with visualization of the flutter stages.

During the fixed-point stability stage, voltages produced were small, less than 1 mV and are thus nonsignificant in terms of harvesting energy. The voltage output of the samples of any given cohort in this stage was the least uniform with sporadic, unsustained oscillations within the samples.

The fixed-point stability regime was demonstrated for low wind speed testing, where large peaks of 60 Hz noise dominated the reading as shown in Fig. 3. Therefore, the amount of energy converted is considered to be negligible.

In samples undergoing the uncoupled MIE stage, sustained vibrations were observed as shown in Fig. 4. The voltage output was increased by about 10x for all tested samples, with one distinct frequency peak. Among samples which experienced this stage, some were observed to undergo chaotic flapping, while others went through LCO-type flutter, and some samples experienced both. LCOs were identified by voltages produced at one narrow frequency, which varied per sample but was of the order of 20 Hz (Fig. 4), and chaotic flapping was characterized by voltages produced at multiple broad frequency ranges (Fig. 5). LCOs occurred often at lower frequencies than those at which chaotic flapping was observed.

The coupled MIE stage occurred when a sample underwent repetitive percussive impact with the top of the test chamber, which acted as a stopper, which created a nonlinear dynamic displacement [18] in the film due to the impact. At lower velocities, only the tip of the sample experienced impact, but as the velocity increased, the length of the sample section striking the chamber wall also increased. The voltage output of this stage was magnitudes greater than that of the uncoupled MIE stage as shown in Fig. 6. The stage of coupled MIE is easy recognized on plots Voltage versus Wind Speed by the rapid growth of voltage of the order of tens or hundreds of mV while uncoupled MIE output is typically between 1 and 10 mV. The large peak voltage was due to the impact of the chamber thus causing large stress in the piezoelectric film. The voltage output in this stage resulted in multiple narrow frequency peaks with decreasing voltage as frequency increased. This was due to the higher frequency caused from the

Table 2 Summary of the variable parameters in the experiment

Parameter	Range of values
Wind speed	0.51–16.47 m/s
Sample length	32–150 mm
Sample width	16 mm, 22 mm
Sample thickness	40 μm, 64 μm

Table 1 Dimensions of each cohort used in the experiment

Dimensional identifier	Length (mm)	Width (mm)	Overall thickness (μm)	Polyvinylidene fluoride thickness (μm)
L32-W16-t40	32	16	40	28
L32-W16-t64	32	16	64	52
L63-W16-t40	63	16	40	28
L63-W16-t64	63	16	64	52
L*xx*-W22-t40	63–150	22	40	28

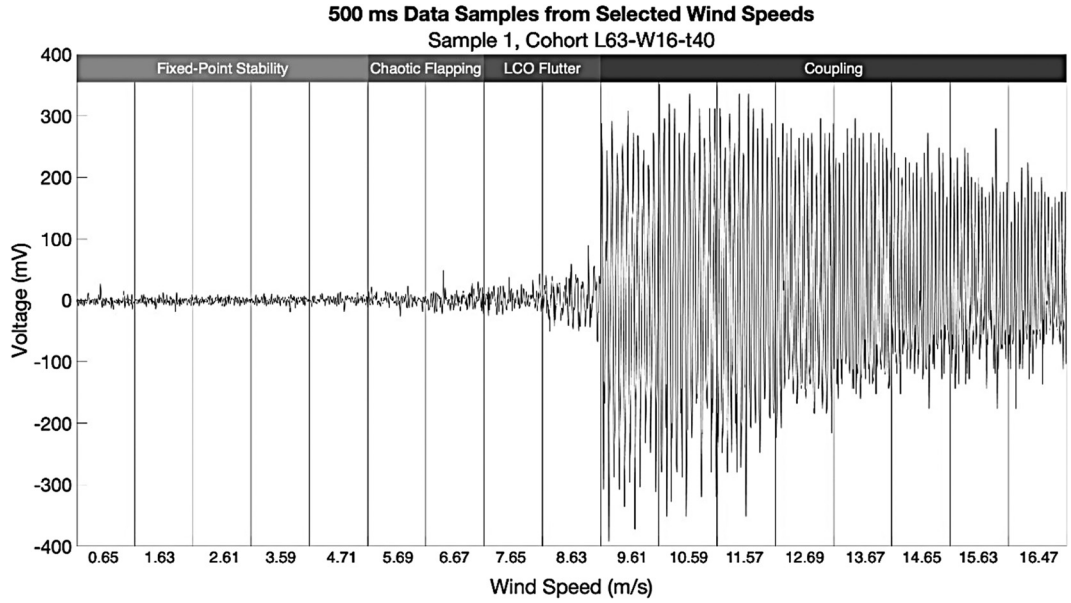

Fig. 2 Voltage variations with time for Sample 1, Cohort L63-W16-t40 undergoing different flutter stages

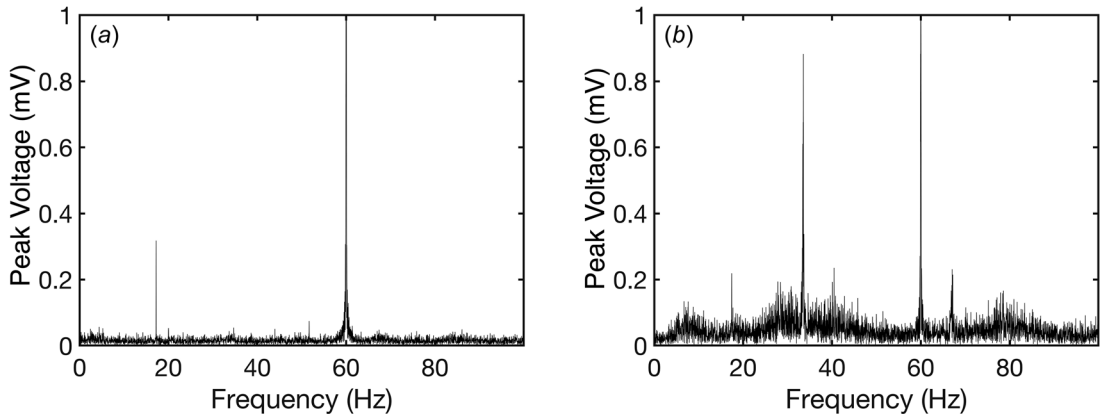

Fig. 3 Voltage versus frequency obtained during the fixed-point stability stage in (*a*) Sample 5 from cohort L63-W16-t40 at 1.77 m/s (an example typical of gentle swaying) and (*b*) Sample 2 from cohort L63-W16-t40 at 3.45 m/s (an example of unsustained oscillations)

impact of the chamber. Therefore, the coupled MIE with piezoelectric film impact was the preferred method of maximizing energy harvesting. Finally, during coupled MIE, the frequencies of each mode increased with wind speed in a linear relationship. As an example, variations of the first and second mode frequencies are shown in Fig. 7.

3.2 Effects of Film Thickness. To test the effects of thickness, samples from two pairs of cohorts, all with a width of 16 mm, were compared. One pair included samples from cohorts L32-W16-t40 and L32-W16-t64. The other pair consisted of cohorts L63-W16-t40 and L63-W16-t64. These cohorts varied the overall thickness from 40 to 64 μm. Figures 8(*a*) and 8(*b*) show a comparison of the mean peak voltages produced by cohorts L32-W16-t40 and L32-W16-t64 with a length of 32 mm. While the samples from L32-W16-t64 produced slightly more voltage than those from the L32-W16-t40 cohort, neither produced a voltage greater than 1 mV as they operated in the fixed-point stability stage at all wind speeds.

Figures 8(*c*) and 8(*d*) investigated the effect of thickness with films of 63 mm in length as these produced coupled MIE regime

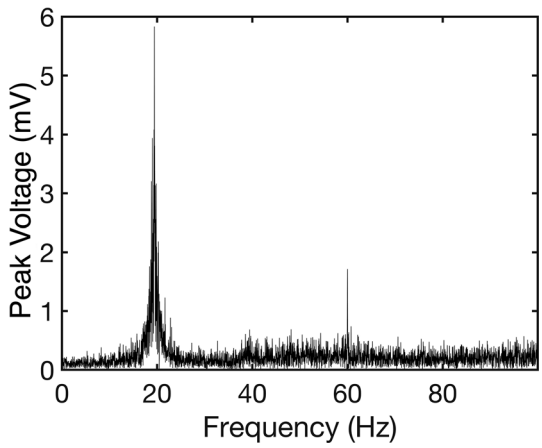

Fig. 4 Voltage versus frequency obtained during the LCO stage in Sample 1 from Cohort L63-W16-t40 at 8.63 m/s. The most prominent feature shows LCO flutter occurring at 19.4 Hz with a magnitude of 5.8 mV.

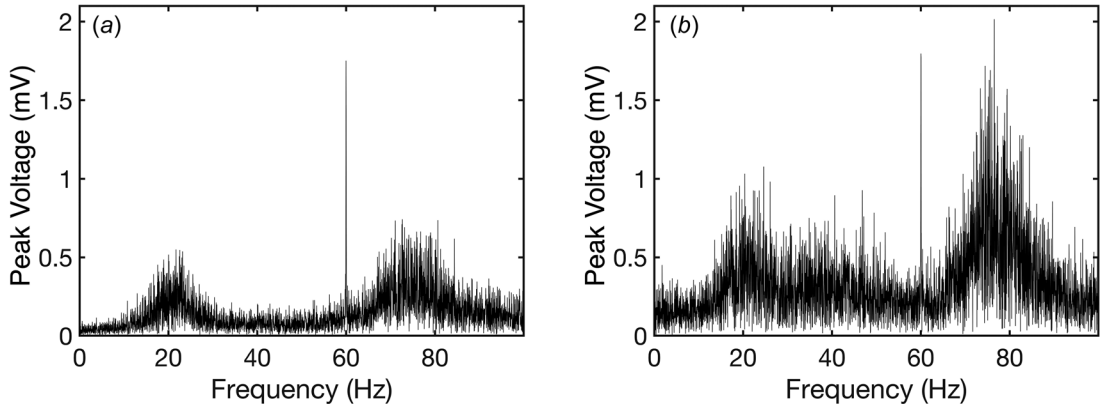

Fig. 5 Voltage versus frequency for (*a*) Sample 2 at 7.79 m/s and (*b*) Sample 4 at 8.07 m/s, both from cohort L63-W16-t40. The dual-peaked broadband frequency response seen in both examples is typical of chaotic flapping observed in this study.

stages. These films demonstrated an increase of sample length had a beneficial effect on the mean peak voltage. Among these samples, the thinner samples from cohort L63-W16-t40 (Fig. 8(*c*)) significantly outperformed those with greater thickness from cohort L63-W16-t64 (Fig. 8(*d*)). In both cohorts, a sharp increase in voltage occurred with the onset of coupled MIE, at 8.65 ± 0.41 m/s for L63-W16-t40, and at 14.37 ± 0.75 m/s for L63-W16-t64. At lower wind speeds, L63-W16-t40 exceeded 1 mV at speeds as low as 3.3 m/s, as illustrated in Fig. 8(*a*), while no samples of L63-W16-t64 exceeded 0.5 mV at speeds below 5.0 m/s. The enhanced performance of the thinner samples was likely due to the decrease in stiffness of the film. A stiffer/thicker film will require greater acceleration to generate the same displacements and stresses as compared to thinner films. This is shown in Fig. 8(*d*) where the increase in voltage occurs at high wind speed, it is believed that higher wind speeds would produce similar voltages as the thinner films in Fig. 8(*c*). Thus, we can conclude that thinner samples will be more efficient for lower wind speeds whereas thicker films can be more efficient for high wind speed conditions. As a result of the earlier onset of coupling, along with better performance at lower wind speeds, the thinner of the two cohorts, L63-W16-t40, was selected for further testing.

3.3 Effects of Film Width. To understand the effects of width, four samples from cohort L63-W22-t40 were tested to compare with cohort L63-W16-t40. In Fig. 9, the average voltages produced by the two cohorts are shown. At wind speeds below 8 m/s, voltages produced by both cohorts were comparable, ranging from approximately 0.4 to 1.5 mV as the wind speed increased (Figs. 9(*a*) and 9(*b*)). However, these operated in the fixed-point stability followed by uncoupled LCO MIE stages. At their coupled MIE onset wind speeds of 8.65 ± 0.41 m/s and 12.44 ± 1.20 m/s, respectively, samples from L63-W16-t40 and L63-W22-t40 showed an increase of orders of magnitude in voltage output. While L63-W16-t40 (Fig. 9(*c*)) had a much lower onset speed than L63-W22-t40 (Fig. 9(*d*)), L63-W22-t40 produced considerably higher voltage, up to 564.9 mV at 16.33 m/s. The maximum voltage output of L63-W16-t40 was only 302.7 mV at 15.91 m/s. These extremes, while interesting, occurred at wind speeds well beyond the range of primary interest of urban wind speeds of 1.3–7.6 m/s. In summary, varying the film width has negligible effects on the film performance at lower wind speeds. This is because altering the width has little effect on the film stiffness. However, the narrower samples experienced the onset of MIE coupling at a lower wind speed than the wider ones likely due to their reduced area and as a result, reduced drag exerted by the airflow on the narrower samples. The wider samples, on the other hand, produced more voltage in the coupled MIE regime at higher wind speeds, because they contain more piezoelectric material. Owing to the similarity of performance within the wind speed range of primary interest, L63-W22-t40 was chosen in addition to L63-W16-t40 for further testing.

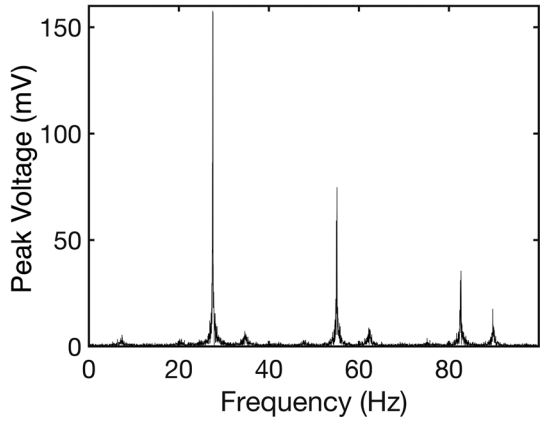

Fig. 6 Voltage versus frequency for cohort L63-W16-t40, Sample 5 at 12.69 m/s

3.4 Effects of Film Length. The effects of varied sample length were ascertained by comparing the voltage production of samples from cohort Lxx-W22-t40 at varied lengths. Three samples were repeatedly cut to increasingly shorter lengths. Sample 1 was tested at lengths 150, 120, 95, and 80 mm. Sample 2 was tested at lengths 130, 110, and 90 mm. Sample 3 was tested once at each length of 70 mm and 63 mm. Samples 2 and 3 were tested with the purpose of increasing the number of tested lengths. Figure 10 demonstrates the performance of the three samples at different lengths in two wind speed ranges: 0.5–9.5 m/s (Figs. 10(*a*) and 10(*b*)) and 5.0–16.5 m/s (Figs. 10(*c*) and 10(*d*)). The sample with the length of 130 mm outperformed others in both velocity intervals. Along with the 150 mm sample, the 130 mm sample experienced the coupled MIE onset at 4.85 m/s. However, at wind speeds below that, the 130 mm sample experienced more productive LCOs than the rest of the samples, its voltage jumping from 0.24 to 0.40 mV between 3.3 and 3.7 m/s (Fig. 10(*a*)). Additionally, at wind speeds within the range of primary interest (1.3–7.6 m/s), the 130 mm sample experienced two voltage peaks of 23.15 and 44.52 mV at 6.7 and 7.6 m/s, respectively, while the 150 mm sample experienced one peak of 12.93 mV at 5.8 m/s. The chamber length was 153 mm which is believed to affect the 150 mm length film.

A possible explanation for this is that as the length of a sample increases, its geometry renders it less stable against the excitation of flutter. However, once a sample exceeds a certain length, in this

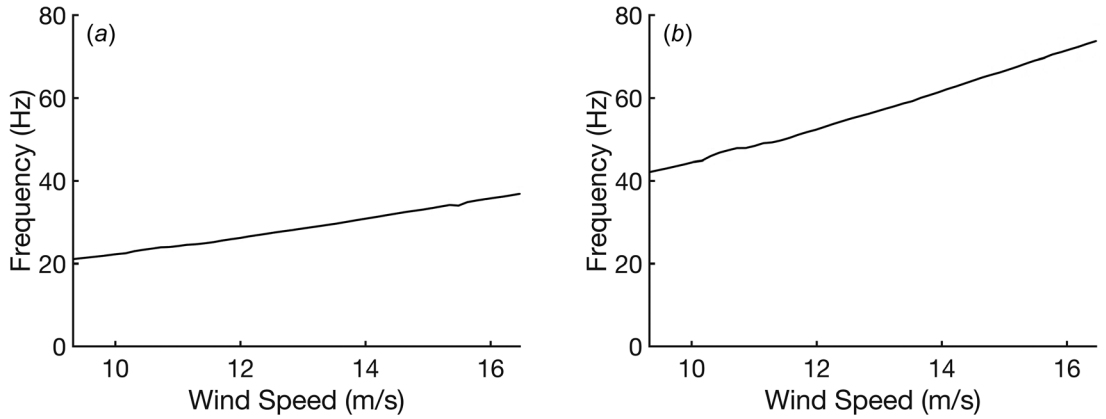

Fig. 7 Dependence of frequencies of (*a*) the first and (*b*) second modes on wind speed for cohort L63-W16-t40 during the coupled MIE stage, with standard deviation error bars

case, 130 mm, damping due to mass begins to overcome such instability. To confirm the performance of the single 130 mm sample, four additional samples of the same length were produced and tested at wind speeds up to 10.03 m/s. The upper limit of 10.03 m/s for wind speeds in this round of testing was chosen because it is above the range of primary interest, 1.3–7.6 m/s, but below the minimum speed of tip damage onset, 12.13 m/s, as discussed below. This round of testing revealed that the overall voltage production of the 130 mm samples (Fig. 11) at this wind speed range (maximum: 122.8 mV at 10.03 m/s) was much greater than that of the 63 mm samples (maximum: 4.61 mV at 9.75 m/s, Figs. 10(*b*) and 10(*d*)) which were tested as part of the sample width comparison, discussed earlier. It is particularly noteworthy that voltage from the 130 mm samples increased by orders of magnitude at 6.49 ± 0.21 m/s, a relatively low onset speed for coupled MIE when compared to other samples in this study. Though it should also be noted that at wind speeds below 3.5 m/s, the 63 mm samples produced three to four times the voltage produced by the 130 mm samples (Figs. 10(*b*) and 10(*d*)). This is likely due to it being easier to excite smaller amounts of material at low wind speeds. To summarize, the voltage production performance of samples from Lxx-W22-t40 improved as length increased, reaching a maximum at 130 mm. This again is believed to be due to the sample stiffness as stiffness decreases as the sample length

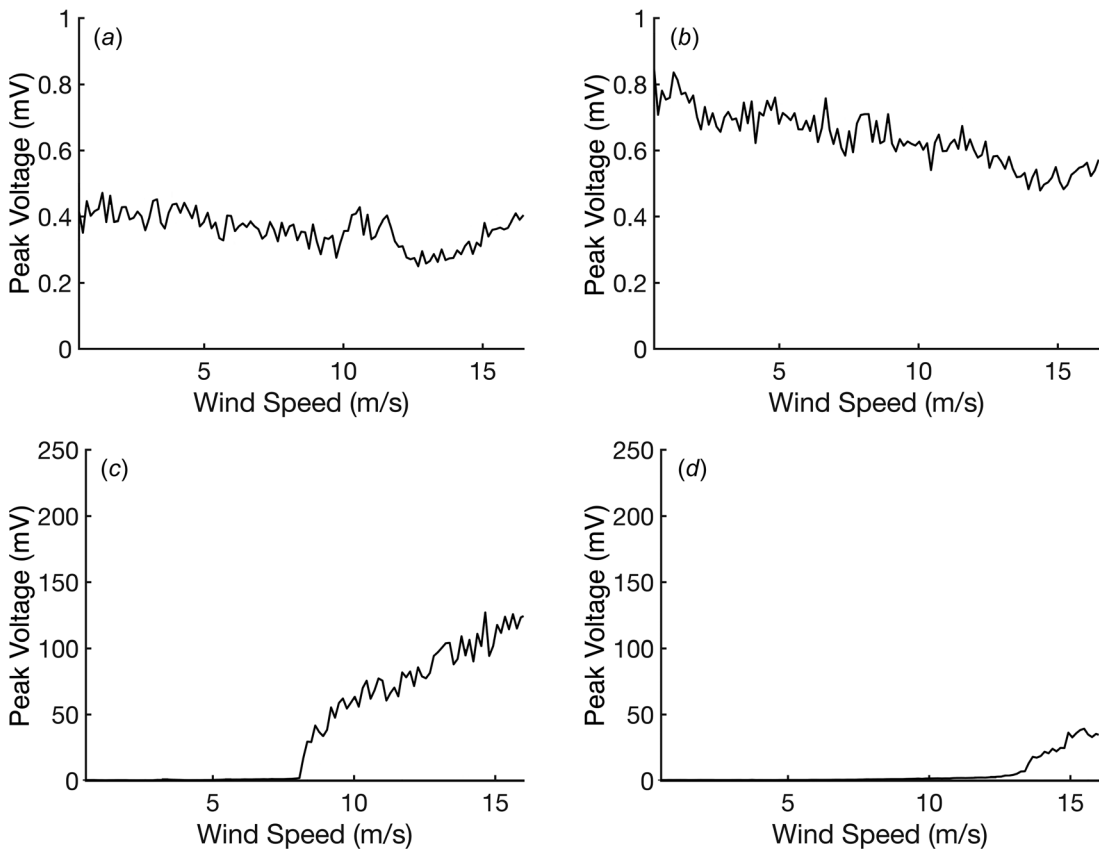

Fig. 8 Comparison of the mean peak voltages of as a function of length and thickness for cohorts (*a*) L32-W16-t40 and (*b*) L32-W16-t64, (*c*) L63-W16-t40, and (*d*) L63-W16-t64

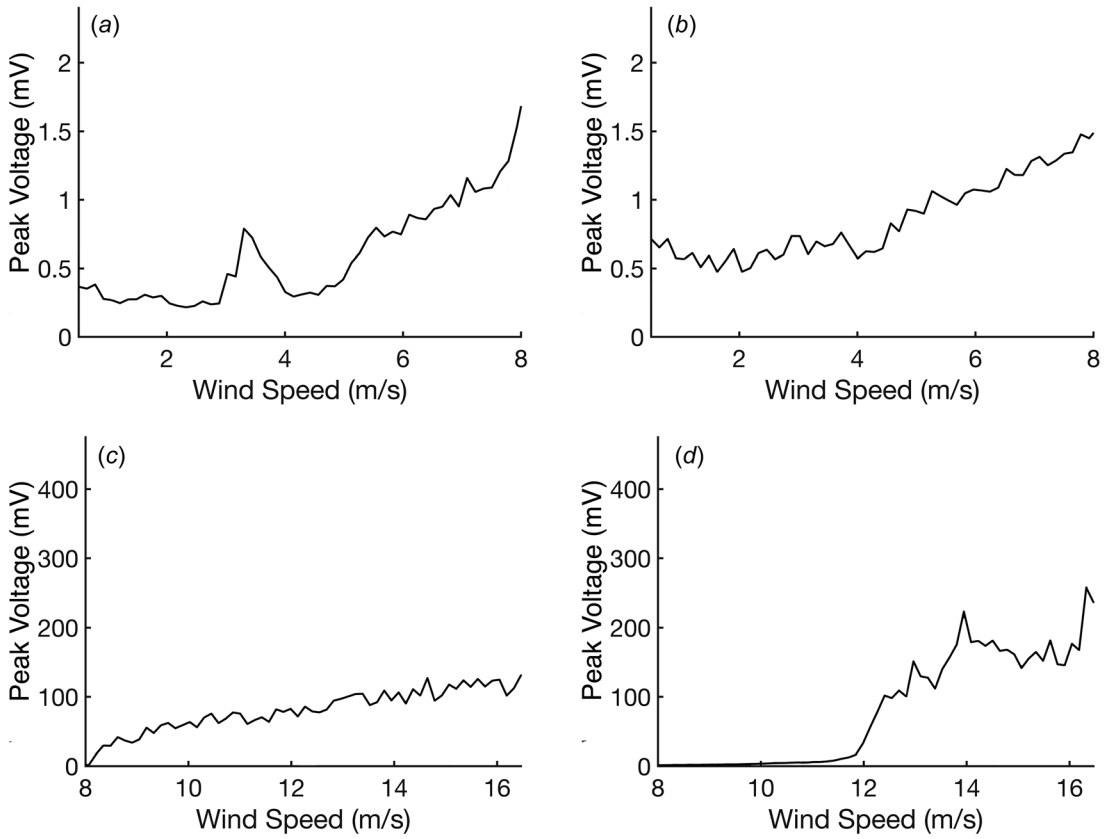

Fig. 9 Average voltages of cohorts (*a*,*c*) L63-W16-t40 and (*b*,*d*) L63-W22-t40 for wind speeds (*a*,*b*) below 8 m/s and (*c*.*d*) above 8 m/s

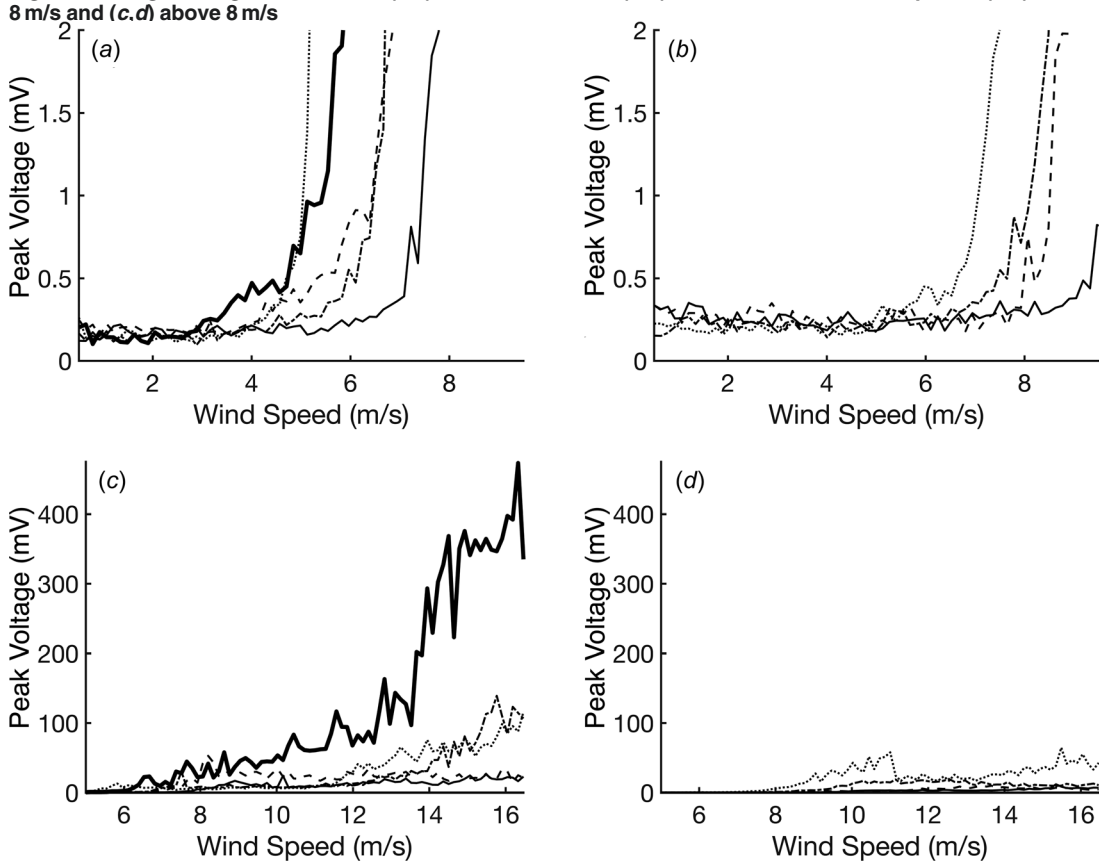

Fig. 10 Voltages produced during testing of multiple sample lengths of cohort Lxx-W22-t40 at different wind speed ranges. Sample lengths tested were (*a*,*c*) 130 mm (thick solid line), 95 mm (solid line), 110 mm (dashed line), 120 mm (dash-dotted line), 150 mm (dotted line); and (*b*,*d*) 63 mm (solid line), 70 mm (dashed line), 80 mm (dash-dotted line), and 90 mm (dotted line).

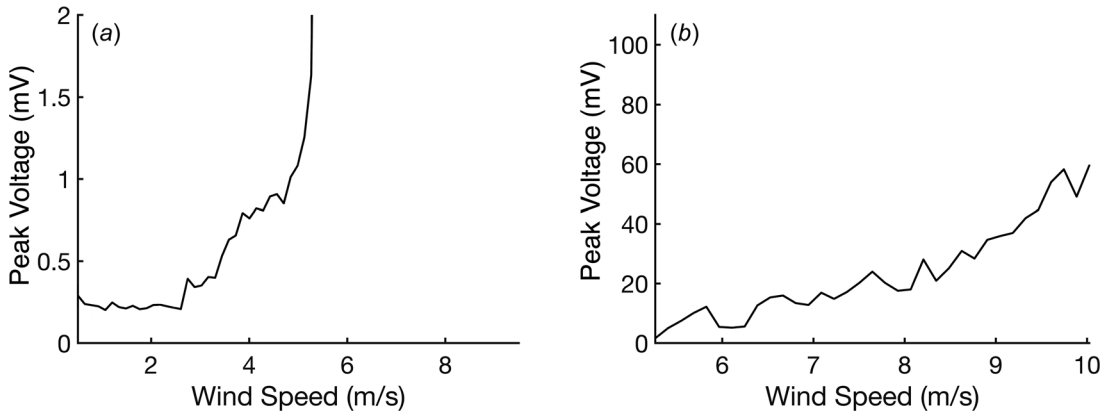

Fig. 11 Mean voltages produced by samples of cohort L130-W22-t40 at wind speeds (*a*) below and (*b*) above 5.3 m/s

increases thus allowing the films to oscillate at lower wind speeds. Thus, samples with a length of 130 mm were selected to be tested for power production.

One observation from conducting experiments described in this section is that at certain high wind speeds, samples with lengths of 90 mm or greater, while experiencing coupled MIE, suffered damage in the form of shredding at their tips, which is due to the impact of film tip to the chamber top. However, since the lowest recorded damage onset speed was 12.13 m/s, well above the range of primary interest, no further consideration to this phenomenon was given and no damage was observed in the experiments described below. However, if coupled MIE is to be used in the future, protective layers at the tip would be necessary for the long-term use of films.

3.5 Power Generation. Based on the results of the previous tests, three cohorts, L63-W16-t40, L63-W22-t40, and L130-W22-t40, were chosen to test for power production. Four samples from each cohort were used in the tests. Figure 12 compares the average power produced by each cohort over the range of wind speeds, 0.5–10.0 m/s. The figure demonstrates that cohort L63-W22-t40 performs the most consistently, producing an average of 0.41 nW, ranging between 0.11 and 0.74 nW (Fig. 12(*b*)). Note that throughout this wind speed range, LCO flutter was observed in this cohort. The other two cohorts only began to match this performance at wind speeds greater than 8 m/s, after the onset of coupled MIE (Figs. 12(*a*) and 12(*c*)). At wind speeds below 8.0 m/s, cohort L130-W22-t40 produced the least power among the three cohorts while in the previous tests, this cohort produced

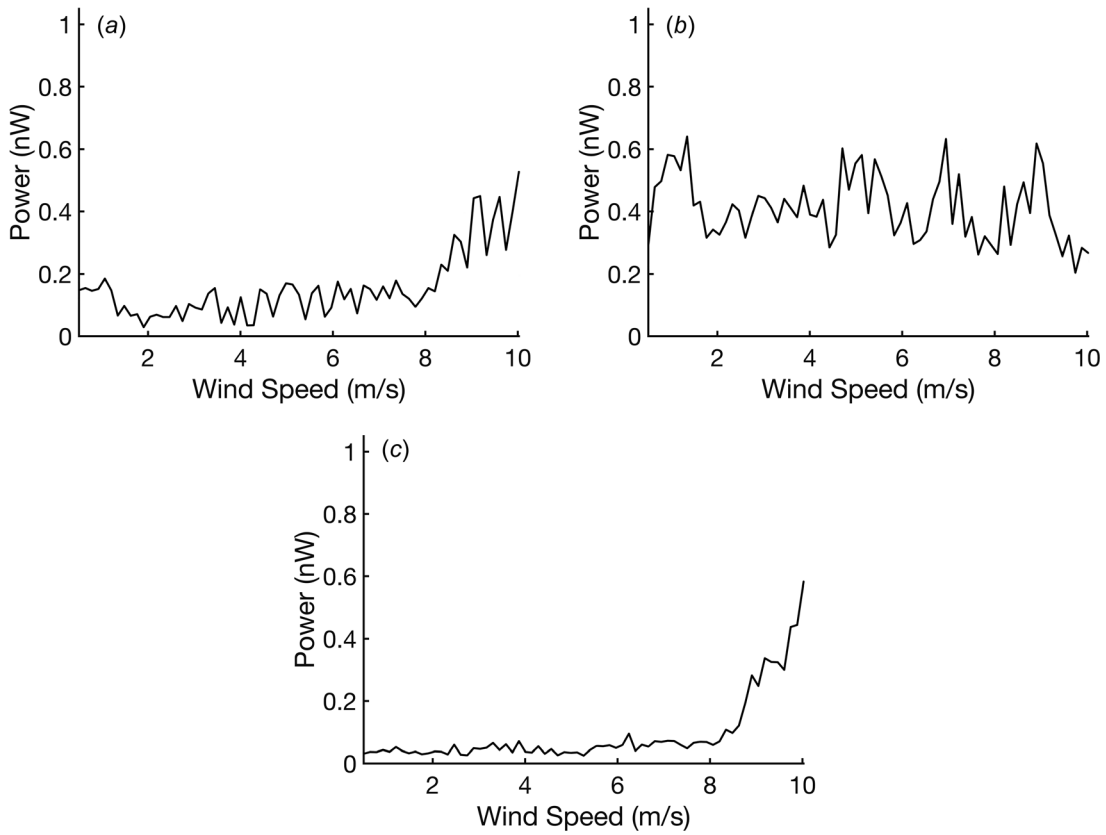

Fig. 12 Power versus wind speed for cohorts (*a*) L63-W16-t40, (*b*) L63-W22-t40, and (*c*) L130-W22-t40

the greatest amount of open-circuit voltage. This is likely due to the phenomenon of damping through resistive shunting [16], wherein the kinetic energy of a piezoelectric element is dissipated through joule heating via ohmic resistance, which has a damping effect on sample vibrations. Indeed, over the course of power testing, samples from cohort L130-W22-t40 were in a circuit with an average resistance of 2.30 ± 0.70 MΩ. On the other hand, cohorts L63-W16-t40 and L63-W22-t40 were incorporated in circuits with resistances of 1.93 ± 0.81 MΩ and 1.62 ± 0.34 MΩ, respectively. As a result, the cohort that was wired with the most resistance produced the least power, and vice versa. Higher power can be harvested using higher wind speeds, which create coupled MIE, and by combining arrays of films.

Here, we will compare results of the current study with those presented previously [20], where two rectangular PVDF samples with dimensions L41-W16-t20 and L171-W22-t20 (in the notations of the current paper) were tested at the wind speed between 3 and 10 m/s. Their shorter sample L41-W16-t20 generated power output in nW (specific values are not provided), which was comparable to our results. However, the longer sample L171-W22-t20 produced much higher power, up to 93.6 μW, than in our study. Whereas the increase in the power production by a longer film observed in [20] is consistent with the findings of this study regarding benefits of using longer samples of the lower stiffness material for the wind energy harvesting, differences in the experimental setups may contribute to different power outputs obtained as the previous studies used samples that were fixed parallel to the flow as opposed to perpendicular to the flow as done in this study. The previous study [20] also used a flow valve to create turbulence. In the current study, the flow was laminarized prior to entering the test chamber.

In summary, results shown in this section suggest the sample length and width of 63 and 22 mm, respectively, to be optimal for power production in the range of wind speeds characteristic for urban areas.

4 Conclusions

In the current study, samples of PVDF films with varying length, width, and thickness in the ranges of 32–150 mm, 16–22 mm, and 40–64 μm, respectively were tested for their voltage and power production utilizing flutter at wind speeds in the range 0.5–16.5 m/s. Three groups of films with dimensions $63\,\text{mm} \times 16\,\text{mm} \times 40\,\mu\text{m}$, $63\,\text{mm} \times 22\,\text{mm} \times 40\,\mu\text{m}$, and $130\,\text{mm} \times 22\,\text{mm} \times 40\,\mu\text{m}$ were found to generate the most voltage. Voltage of interest from practical perspective was created by the excitation of flutter in the form of uncoupled LCO MIE and coupled MIE. While LCOs consistently produced voltages ranging from 1 to 10 mV, coupled MIE typically produced voltages in the 100's of mV range. However, coupled MIE typically occurs at wind speeds outside the range of wind speeds in urban areas. To enable coupled MIE at lower wind speeds, piezoelectric films with reduced thickness, low elastic modulus, and increased length are desired. Novel flexible polymers with lower elastic moduli would be beneficial for this application.

Comparing the power production by these three groups of films, films with dimensions $63\,\text{mm} \times 22\,\text{mm} \times 40\,\mu\text{m}$ (cohort L63-W22-t40), produced the most power, 0.41 ± 0.32 nW, within the wind speed range of primary interest, 1.3–7.6 m/s, throughout which LCO flutter was observed. While power produced even by the best single strip was low (maximum: 0.74 nW), the films are expected to be assembled in arrays rather than to be utilized individually. Results presented in the current paper for the individual films are meant to facilitate the design of such arrays.

Funding Data

- University of New Mexico Women in STEM Faculty Development Fund.
- National Science Foundation EPSCoR Cooperative Agreement OIA-1757207.

References

[1] Jose, Z., Michael, D., Patrick, G., Ananthan, S., Lantz, E., Cotrell, J., 2015. Enabling wind power nationwide. U.S. Department of Energy. https://www.energy.gov/sites/prod/_les/2015/05/f22/Enabling%20Wind%20Power%20Nationwide 18MAY2015 FINAL.pdf

[2] André, D., Grove, J., Grossman, L., Moynihan, S., and Raker, J., 2006. Community Wind: An Oregon Guidebook. Prepared for the Energy Trust of Oregon by the Northwest Sustainable Energy. https://www.energytrust.org/wp-content/uploads/2016/10/cwpgcommwindguidebook.pdf

[3] Bornstein, R. D., and Johnson, D. S., 1977, "Urban-Rural Wind Velocity Differences," Atmos. Environ. (1967), **11**(7), pp. 597–604.

[4] Frazer, R. A., 1929, "The Flutter of Aeroplane Wings," Aeronaut. J., **33**(222), pp. 407–454.

[5] Baumhauer A. G, V., and Koning, C., 1923. On the Stability of Oscillations of an Airplane Wing. NACA Technical Memorandum No. 223, August 1923. https://ntrs.nasa.gov/archive/nasa/casi.ntrs.nasa.gov/19930084621.pdf

[6] Akaydin, H., Elvin, N., and Andreopoulos, Y., 2012, "The Performance of a Self-Excited Fluidic Energy Harvester," Smart Mater. Struct., **21**(2), p. 025007.

[7] Akaydin, H. D., Elvin, N., and Andreopoulos, Y., 2010, "Energy Harvesting From Highly Unsteady Fluid Flows Using Piezoelectric Materials," J. Intell. Mater. Syst. Struct., **21**(13), pp. 1263–1278.

[8] Bae, J., Lee, J., Kim, SMin., Ha, J., Lee, B.-S., Park, YJun., Choong, C., Kim, J.-B., Wang, Z. L., Kim, H.-Y., Park, J.-J., and Chung, U.-I., 2014, "Flutter-Driven Triboelectrification for Harvesting Wind Energy," Nat. Commun., **5**(1), pp. 1–9.

[9] Çevik, G., Akşit, M. F., and Şabanoviç, A., 2011, "Piezoelectric Wind Power Harnessing–an Overview," Proceedings of the SET2011, 10th International Conference on Sustainable Energy Technologies, Istanbul, Turkey, Sept. 4–7.

[10] Hobbs, W. B., and Hu, D. L., 2012, "Tree-Inspired Piezoelectric Energy Harvesting," J. Fluids Struct., **28**, pp. 103–14.

[11] Hobeck, J., and Inman, D., 2012, "Artificial Piezoelectric Grass for Energy Harvesting From Turbulence-Induced Vibration," Smart Mater. Struct., **21**(10), p. 105024.

[12] Hobeck, J. D., Energy Harvesting with Piezoelectric Grass for Autonomous Self-Sustaining Sensor Networks, 2014.

[13] Hobeck, J. D., Geslain, D., and Inman, D. J., 2013, "The Dual Cantilever Flutter Phenomenon: A Novel Energy Harvesting Method," Proceedings of the SPIE 9061, Sensors and Smart Structures Technologies for Civil, Mechanical, and Aeroscape Systems, April 10, 906113. http://proceedings.spiedigitallibrary.org/proceeding.aspx?doi=10.1117/12.2061051

[14] Kwon, S.-D., 2010, "A T-Shaped Piezoelectric Cantilever for Fluid Energy Harvesting," Appl. Phys. Lett., **97**(16), p. 164102.

[15] Li, S., Yuan, J., and Lipson, H., 2011, "Ambient Wind Energy Harvesting Using Cross-Flow Fluttering," J. Appl. Phys., **109**(2), p. 026104.

[16] McCarthy, J., Energy capture from ambient flows using piezoelectric flutter harvesters, Ph.D. thesis, 2014, RMIT University, Melbourne, Australia.

[17] McCarthy, J., Deivasigamani, A., John, S., Watkins, S., Coman, F., and Petersen, P., 2013, "Downstream Flow Structures of a Fluttering Piezoelectric Energy Harvester," Exp. Therm. Fluid Sci., **51**, pp. 279–290.

[18] Morris, D. L., Wind generated electricity using flexible piezoelectric materials, M.S. thesis, 2010, The University of Minnesota, Minneapolis, MN.

[19] Sward, J., Scott, P. C., Wayne, P., Jackson, N., Vorobieff, P., Lumia, R., and Poroseva, S. V., 2020, "Harvesting Energy From an Ionic Polymer–Metal Composite in a Steady Air Flow," ASME J. Fluids Eng., **142**(8), p. 081204.

[20] Vatansever, D., Hadimani, R., Shah, T., and Siores, E., 2011, "An Investigation of Energy Harvesting from Renewable Sources With PVDF and PZT," Smart Mater. Struct., **20**(5), p. 055019.

[21] Wang, W., He, X., Wang, X., Wang, M., and Xue, K., 2018, "A Bioinspired Structure Modification of Piezoelectric Wind Energy Harvester Based on the Prototype of Leaf Veins," Sens. Actuators A: Phys., **279**, pp. 467–473.

[22] Weinstein, L. A., Cacan, M. R., So, P., and Wright, P., 2012, "Vortex Shedding Induced Energy Harvesting From Piezoelectric Materials in Heating, Ventilation and Air Conditioning Flows," Smart Mater. Struct., **21**(4), p. 045003.

[23] Zhao, L., and Yang, Y., 2017, "On the Modeling Methods of Small-Scale Piezoelectric Wind Energy Harvesting," Smart Struct. Syst., **19**(1), pp. 67–90.

[24] Naudascher, E., and Rockwell, D., 1994, *Flow-Induced Vibrations: An Engineering Guide*, A.A. Balkema, Rotterdam; Brookfield, VT.

[25] Carroll, C. B., 2002, Energy harvesting eel. Google Patents.

[26] Liu, H., Lee, C., Kobayashi, T., Tay, C. J., and Quan, C., 2012, "Investigation of a MEMS Piezoelectric Energy Harvester System With a Frequency-Widened-Bandwidth Mechanism Introduced by Mechanical Stoppers," Smart Mater. Struct., **21**(3), p. 035005.

[27] Olszewski, O. Z., Houlihan, R., Blake, A., Mathewson, A., and Jackson, N., 2017, "Evaluation of Vibrational PiezoMEMS Harvester That Scavenges Energy From a Magnetic Field Surrounding an AC Current-Carrying Wire," J. Microelectromech. Syst., **26**(6), pp. 1298–1305.

[28] Fei, F., Zhou, S., Mai, J. D., and Li, W. J., 2014, "Development of an Indoor Airflow Energy Harvesting System for Building Environment Monitoring," Energies, **7**(5), pp. 2985–3003.

[29] Jackson, N., Kumar, K., Olszewski, O., Schenning, A. P., and Debije, M. G., 2019, "Tuning MEMS Cantilever Devices Using Photoresponsive Polymers," Smart Mater. Struct., **28**(8), p. 085024.

[30] Jackson, N., Olszewski, O. Z., O'Murchu, C., and Mathewson, A., 2017, "Shock-Induced Aluminum Nitride Based MEMS Energy Harvester to Power a Leadless Pacemaker," Sens. Actuators A: Phys., **264**, pp. 212–8.
[31] Jackson, N., Olszewski, O. Z., O'Murchu, C., and Mathewson, A., 2018, "Ultralow-Frequency PiezoMEMS Energy Harvester Using Thin-Film Silicon and Parylene Substrates," J. Micro/Nanolithography, MEMS, MOEMS, **17**(1), p. 1.
[32] Liu, H., Tay, C. J., Quan, C., Kobayashi, T., and Lee, C., 2011, "Piezoelectric MEMS Energy Harvester for Low-Frequency Vibrations With Wideband Operation Range and Steadily Increased Output Power," J. Microelectromech. Syst., **20**(5), pp. 1131–1142.
[33] Jackson, N., Keeney, L., and Mathewson, A., 2013, "Flexible-CMOS and Biocompatible Piezoelectric AlN Material for MEMS Applications," Smart Mater. Struct., **22**(11), p. 115033.
[34] Jackson, N., and Mathewson, A., 2017, "Enhancing the Piezoelectric Properties of Flexible Hybrid AlN Materials Using Semi-Crystalline Parylene," Smart Mater. Struct., **26**(4), p. 045005.
[35] Ramadan, K. S., Sameoto, D., and Evoy, S., 2014, "A Review of Piezoelectric Polymers as Functional Materials for Electromechanical Transducers," Smart Mater. Struct., **23**(3), p. 033001.
[36] Shan, X., Tian, H., Chen, D., and Xie, T., 2019, "A Curved Panel Energy Harvester for Aeroelastic Vibration," Appl. Energy, **249**, pp. 58–66.
[37] Zhang, J., Zhang, J., Shu, C., and Fang, Z., 2017, "Enhanced Piezoelectric Wind Energy Harvesting Based on a Buckled Beam," Appl. Phys. Lett., **110**(18), p. 183903.
[38] Connell, B. S., and Yue, D. K., 2007, "Flapping Dynamics of a Flag in a Uniform Stream," J. Fluid Mech., **581**, pp. 33–67.